PAPER

Monodisperse platinum nanoparticles supported on highly ordered mesoporous silicon nitride nanoblocks: superior catalytic activity for hydrogen generation from sodium borohydride†

Chrystelle Salameh,[a] Alina Bruma,[b] Sylvie Malo,[b] Umit B. Demirci,[a] Philippe Miele[a] and Samuel Bernard*[a]

Late transition metal have attracted considerable interest for catalytic applications. Their immobilization over supports with tailored porosity is advantageous for nanosizing metal particles and avoiding their agglomeration which is known to bring a serious issue to the catalytic performance. Herein, ordered mesoporous silicon nitride (Si_3N_4) nanoblocks with hexagonal symmetry of the pores, high specific surface areas (772.4 m^2 g^{-1}) and pore volume (1.19 cm^3 g^{-1}) are synthesized by nanocasting using perhydropolysilazane as precursor. Then, Si_3N_4 nanoblocks are used as supports to synthesize platinum nanoparticles (Pt NPs) by precursor wet impregnation. Detailed characterizations by TEM show that monodispersed spherical Pt NPs with a 6.77 nm diameter are successfully loaded over nanoblocks to generate nanocatalysts. The latter are subsequently used for the catalytic hydrolysis of sodium borohydride ($NaBH_4$). A hydrogen generation rate of 13.54 L min^{-1} g_{Pt}^{-1} is measured. It is notably higher than the catalytic hydrolysis using Pt/CMK-3 nanocatalysts (2.58 L min^{-1} g_{Pt}^{-1}) most probably due to the textural properties of the Si_3N_4 supports associated with the intrinsic properties of Si_3N_4. This leads to an attractive nanocatalyst in pursuit of practical implementation of B-/N-based chemical hydrides as a hydrogen source for fuel cell application.

A   Introduction

Proton exchange membrane fuel cell-based (PEMFC) systems are attractive alternatives to current energy conversion technologies due to their potential to directly convert chemical energy (*i.e.*, hydrogen) into electrical energy. They consist of three subsystems – fuel cell stack, hydrogen generator, and hybrid power management system. They display high efficiency, fast responses to loads and they have potentially zero emissions (except water).[1,2] However, despite recent advances, there are still several issues which limit the widespread use of the fuel cell technologies. One of the key challenges is the controlled release of hydrogen to meet the overall energy requirements for civil vehicle applications such as for small Unmanned Aerial Vehicles (UAVs) commonly known as drones. For this purpose, liquid-phase hydrogen carriers are attractive, owing to some very advantageous features:[3] they are in liquid state (especially

in aqueous solution), and thus can be easily handled, they are relatively stable in ambient conditions, non-flammable, non-toxic, they are hydrogen-rich compounds and side-products are recyclable. A typical and widely-investigated example is the alkaline solution of sodium borohydride $NaBH_4$.[4]

$NaBH_4$ carries 10.8 wt% of hydridic ($H^{\delta-}$) hydrogen. Hydrogen can be easily released by reaction with the protic ($H^{\delta+}$) hydrogen of water, which thus provides half of the hydrogen H_2 generated. The hydrolysis has to be accelerated by a metal-based catalyst.[5–9] As an illustration, effective gravimetric hydrogen storage capacities up to 9 wt% can be achieved in the presence of a supported catalyst.[8] However, such attractive performances imply harsh operating conditions such as high temperatures (*e.g.* 80–100 °C) or high pressures (*e.g.* >6 bars H_2). These studies demonstrate that both the catalyst and the support play a key role in the production of H_2 from $NaBH_4$ to withstand these harsh conditions.

Late transition metals like ruthenium (Ru) or platinum (Pt) are generally more active and stable than cobalt (Co)[10–12] but the cost issue is a limiting factor. Therefore, catalytic application requires significant reduction in the amount of expensive metal while catalytic performance is expected to be enhanced. It is therefore crucial to use very low amounts of metals ($\leq$1 wt%) in the form of nanoparticles (NPs) in order to optimize catalytic

[a]IEM (Institut Europeen des Membranes), UMR 5635 (CNRS-ENSCM-UM), Universite Montpellier, Place E. Bataillon, F-34095, Montpellier, France. E-mail: Samuel.Bernard@univ-montp2.fr; Fax: +33 467 149 119; Tel: +33 467 149 159

[b]CRISMAT Laboratory, UMR 6508 (CNRS-ENSICAEN-UNICAEN), 6 Bld Marechal Juin, 14050, Caen, France

† Electronic supplementary information (ESI) available. See DOI: 10.1039/c5ra05901a

activities. However, the nanoparticles agglomeration is problematic during the long-term catalytic process, bringing a serious issue to the catalyst stability. Consequently, the active surface areas of Pt NPs are continuously destroyed, resulting in continuous catalyst degradation with aging. An efficient solution is the immobilization of the catalyst over a support.[13] The resulting dispersed particles exhibit a much higher total surface area per unit weight than the bulk metal, therefore allowing better utilization of the metal as a result of dispersion.

In general, the specific surface area, the pore volume, the arrangement and type of the porosity as well as the Lewis and/or Brønsted acidity of materials are primarily considered when selecting a support for catalysts to be used in H_2 generation. The thermal conductivity, mechanical strength and especially the chemical resistance towards the reaction medium are not always viewed as the most important properties. Alumina, silica, zeolites and MOFs are generally used as catalyst supports for various catalytic reactions.[14–19] As an illustration, silica has been used as a support for the catalytic hydrolysis of ammonia borane.[20] However, the application of silica, zeolites, metal oxides or MOFs in catalytic hydrolysis is somehow limited because their hydrothermal stability may turn to be poor in the severe conditions we have imposed in our study, leading in general to the collapse of the porous structure. To address the issue of highly stable supports to produce H_2 from the alkaline solution of $NaBH_4$, alternative support materials should be explored.

Carbonaceous supports may represent an alternative solution. However, silicon carbide (SiC) and silicon nitride (Si_3N_4) attract much more attention, primarily due to their good mechanical and particularly chemical properties, their high thermal stability and their relative high thermal conductivity. Up to now, one group has investigated the use of Si_3N_4 as a non-porous powdered support (specific surface area < 60 m^2 g^{-1}) of metals (Ag, Pd, Pt, *etc.*), in particular for the catalytic oxidation of methane and alcohols.[21–25] In order to better control the size of the particle and avoid the sintering of the metals which inherently occurs on non-porous supports, development of porosity is required.

The Polymer-Derived Ceramics (PDCs) route has been widely investigated to prepare non-oxide ceramics with a tailored porosity.[26–38] In contrast, reports focused on their use as supports are extremely limited. There are two strategies to prepare metal-supported porous PDCs. The basis of the first strategy is to mix in a controlled molar ratio a metal-containing molecule with a polymeric precursor to generate a metal-containing polymer. This synthesis strategy, usually investigated to produce ceramic–ceramic nanocomposites,[39] is directed to produce metal–ceramic nanocomposites after pyrolysis during which *in situ* controlled growth of metal occurs in the matrix.[26–29] From a chemistry point of view, the strategy, developed particularly in ref. 28, is very promising and allows producing various compositions of nanocomposites. This molecular approach is advantageous owing to the dispersion of the metal at an atomic level, and the broad applicability (coordination compounds of many metals can be used). As an illustration, using nickel (Ni) as metal, particles seem to be
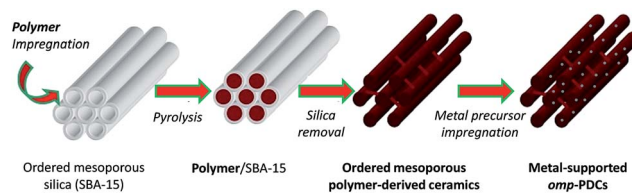

Fig. 1 Procedure to prepare metal-supported PDCs using SBA-15 as template.

located near the external surface of the nanocomposites and within the internal voids and therefore the nanocomposites demonstrate catalytic activity for hydrogenation reactions.[28b,d] Despite these very recent advances and the possibility to prepare the targeted nanocatalysts within one step,[28b,d] we focused on the second strategy that consists into the replication of the porous structure of templates such as SBA-15 (or CMK-3 in our case) by polymer nanocasting.[35,36] As-obtained materials with tailored porosity are impregnated with the metal precursor in order to be chemically reduced (Fig. 1). This allowed to (i) tune the porosity much more effectively, (ii) fully convert the preceramic polymers into ceramics (which is relatively difficult when metals and ceramics are prepared together in the same composite), (iii) optimize chemical and thermal stability and (iv) avoid possible reactions between the metal and the matrix (formation of metal silicides[28c]).

In this general context, we propose herein the synthesis and characterization of a new class of ordered mesoporous Si_3N_4 labelled *omp*-Si_3N_4 in the form of nanoblocks with hexagonal symmetry, very high specific surface area and large pore volume by perhydropolysilazane nanocasting, followed by platinum nanoparticle growth leading second to the generation of new nanocatalysts labelled Pt/*omp*-Si_3N_4 (Fig. 2).

Finally, these nanocatalysts were tested for H_2 generation by hydrolysis of $NaBH_4$. The performance is compared to the H_2 evolution over other nanocatalysts[40] to extrapolate and highlight the performance in the catalytic activity of the new Si_3N_4-based nanocatalysts.
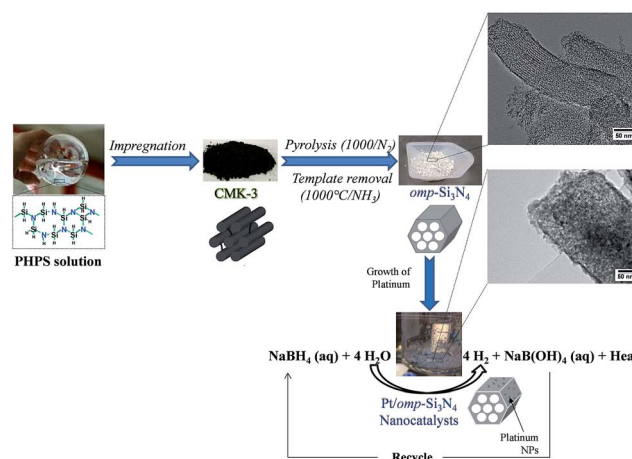

Fig. 2 Overall process for preparing Pt/*omp*-Si_3N_4.

B   Experimental part

A   Materials

The polymeric precursor is unstable in air. Therefore, all manipulations are carried out under inert conditions. All ceramic products are handled in an argon-filled glove box (MBraun MB200B; O_2 and H_2O concentrations kept at <0.1 ppm) due to their high surface area and affinity for moisture before characterization. Argon (>99.995%) is purified by passing through successive columns of phosphorus pentoxide, sicapent™, and BTS catalysts. Schlenk tubes are dried at 120 °C overnight before pumping under vacuum and filling them with argon for synthesis. CMK-3 was purchased from ACS Materials®. Textural and structural parameters are reported in Table 1. Further information concerning CMK-3 are provided in the website of ACS Material®.

Perhydropolysilazane in xylene (20 wt%) (PHPS, AQUAMICA NN-310) is provided by Mitsuya Boeki Ltd., Japan. Anal. found (wt%): Si, 65.1; N, 26.2; H, 8.3; O, 0.4. FTIR (KBr/cm^{-1}): ν(N–H) = 3374 (m), ν(Si–H) = 2125 (s), ν(N–H) = 1180 (s), ν(Si–N) = 840–1020 (s). ^{1}H NMR (300 MHz, C_6D_6, δ/ppm): 1.6–0.3 (NH), 5.8–4.3 (SiH). ^{29}Si NMR (79.43 MHz, C_6D_6, δ/ppm): −39.0 ppm (HSiN$_3$/ H$_2$SiN$_2$).

For the preparation of the Pt supported samples and the hydrogen generation experiments, chloroplatinic acid hexahydrate ($H_2PtCl_6 \cdot 6H_2O$, Sigma-Aldrich), sodium borohydride ($NaBH_4$, Acros Organics), sodium hydroxide (NaOH, Carlo Erba) and deionized ultra-pure water (Milli-Q grade; resistivity > 18 MΩ cm) are used.

B   Preparation of ordered mesoporous silicon nitride nanoblocks

Nanocasting of PHPS is carried out through an impregnation process in a Schlenk-type flask. 4.5 mL of the PHPS dissolved in xylene under stirring are added to 0.63 g of the CMK-3 template dehydrated at 150 °C overnight at reduced pressure prior to use. The mixture is then stirred at 10 °C for 48 h under static vacuum. After absorption of the polymer into the pores of the template, a filtration step is performed and then the solvent is evaporated at low pressure at 30 °C to generate a black powder labeled PHPS/CMK-3. The dried composite is transferred into a silica tube inserted in a horizontal tube furnace (Nabertherm type RS 80/500/11, Germany) connected to a nitrogen-filled glove-box. Subsequently, the PHPS/CMK-3 composite is subjected to a N_2 cycle of ramping of 1 °C min^{-1} to 1000 °C, dwelling there for 2 h, and then cooling to RT at 2 °C min^{-1}. After the polymer-to-ceramic conversion process, the composite undergoes a final thermal treatment under NH_3 through a cycle of ramping of 5 °C min^{-1} to 1000 °C, dwelling there for 5 h, and then cooling to RT at 5 °C min^{-1} to generate samples *omp*-Si_3N_4.

C   Preparation of platinum-supported silicon nitride

Sodium hydroxide and sodium borohydride are used as received, the latter being handled in the argon-filled glove-box. The platinum nanoparticles synthesized from the precursor $H_2PtCl_6 \cdot 6H_2O$ are supported over *omp*-Si_3N_4 by wet impregnation followed by sodium hydroxide-assisted chemical reduction using aqueous $NaBH_4$. Typically, 43 mg of *omp*-Si_3N_4 are milled, transferred in 2.5 mL of water, and ultrasonicated for 1 h in ambient conditions. Then, 1 mL of an aqueous solution of $H_2PtCl_6 \cdot 6H_2O$ (2.44×10^{-3} M) are added to the dispersion of *omp*-Si_3N_4. The mixture is further ultrasonicated for 1 h. Meanwhile, the reducing solution (*i.e.* alkaline aqueous solution of $NaBH_4$, with the concentrations of NaOH and NaBH4 being of 3 M and 0.14 M, respectively) is prepared. It is added dropwise to the mixture Pt^{4+}(aq) + *omp*-Si_3N_4 while the solution was vigorously shaken; the total time of addition is fixed to 30 min. As a final step, the solution is filtrated, and the solid washed twice with deionized water, washed with ethanol, and dried at 60 °C to generate Pt/*omp*-Si_3N_4. For comparison, Pt/*omp*-Si/Al/C/N[40] and Pt/CMK-3 has been prepared following the same experimental procedure. 103 mg of CMK-3 are milled, transferred in 3.5 mL of distilled water, and ultrasonicated for 1 h in ambient conditions. Then, 1 mL of an aqueous solution of $H_2PtCl_6 \cdot 6H_2O$ (2.44×10^{-3} M) are added to the dispersion of CMK-3.

D   Characterization

PHPS was analyzed by FTIR spectroscopy using a Nicolet Magna 550 spectrometer. ^{1}H and ^{29}Si NMR data of PHPS were obtained using a Bruker AM 300 spectrometer in C_6D_6 operating at 300 MHz and 79.43 MHz, respectively. Tetramethylsilane (TMS) was used as a reference. Thermogravimetric analyses (TGA) of the polymer-to-ceramic conversion are recorded on a Setaram TGA 92 16.18. Experiments are performed at 5 °C min^{-1} up to 1000 °C (dwelling time of 5 h) under ammonia using silica crucibles (sample weight of ~40 mg) at ambient atmospheric pressure. The Small-Angle powder X-Ray Diffraction pattern (SA-XRD) is recorded using a Philips PW 3040/60 X'Pert PRO X-ray diffraction system operating at 30 mA and 40 kV, and between 0.5° and 2.5° with a step size of 0.0167°. In addition, powder X-ray diffraction is applied from 20° to 80° to identify the global structure of the Si_3N_4 phase. SAXS (Small Angle X-ray Scattering) and WAXS (Wide Angle X-ray Scattering) experiments are performed with an in-house setup of the *Laboratoire Charles Coulomb, "Réseau X et gamma", Université Montpellier 2, France*.

Table 1   Textural properties of CMK-3

Type	SSA [m^2 g^{-1}]	Pore diameter [nm]	Total pore volume [cm^3 g^{-1}]	Micropore volume [cm^3 g^{-1}]	Size [μm]
BET1000	983	5.57	1.35	0.01	0.5–5

A high brightness low power X-ray tube, coupled with aspheric multilayer optic (GeniX^{3D} from Xenocs) was employed. It delivers an ultralow divergent beam (0.5 mrad). Scatterless slits were used to give a clean 0.8 mm beam diameter (35 Mphotons per s) at the sample. We worked in a transmission configuration and scattered intensity was measured by a Schneider 2D image plate detector prototype, at a distance of 1.9 m from the sample for SAXS configuration, 0.2 m from the sample for WAXS configuration. All intensities are corrected by transmission and the empty cell contribution is subtracted. The mesoporous materials are observed by SEM (Hitachi S800) equipped with energy-dispersive spectroscopy analysis (EDXS). The Brunauer–Emmett–Teller (BET) method was used to calculate the specific surface area of samples. The pore-size distribution is derived from the desorption branches of the isotherms using the Barrett–Joyner–Halenda (BJH) method. The total pore volume (V_p) is estimated from the amount of N_2 adsorbed at a relative pressure of (P/P_0) 0.97. Samples for TEM are ground in ethanol and the resulted dispersion was transferred to a lacey or holey carbon film fixed on a 3 mm nickel grid. High-resolution TEM (HRTEM) and electron diffraction (ED) studies are performed using a FEI Tecnai G^2 30 UT (LaB$_6$) microscope operating at 300 kV with a 0.17 nm point resolution. The catalytic ability of Pt/ *omp*-Si$_3$N$_4$ is assessed in hydrogen production by hydrolysis of sodium borohydride in our 'harsh' conditions, and the hydrogen generation measurement is performed according to the general procedure we reported in ref. 41. Typically, the catalyst (16 mg) is milled and sieved, and then transferred into a reactor (glass tube) that is sealed with a silicon septum. The reactor is connected to a water-filled inverted burette (water colored in blue), *via* a cold trap for steam, maintained at 0 °C. Then, it is immersed in an oil bath kept at 80 °C. To start the hydrogen generation, 1 mL of a stabilized (2 wt% NaOH) aqueous solution of NaBH$_4$ (120 mg) is injected over the catalyst. Hydrogen starts to evolve rapidly and the evolution is video-recorded for 2 h, to be then computationally analyzed post-hydrolysis.

C Results and discussion

A Preparation of ordered mesoporous Si$_3$N$_4$ nanoblocks

We report the synthesis of highly ordered mesoporous Si$_3$N$_4$ with a hexagonal lattice from perhydropolysilazane (PHPS, [SiH$_2$–NH]$_n$). PHPS is a highly reactive preceramic polymer containing two Si–H and N–H functions in its structure.[39a,42–46] Through pyrolysis under nitrogen, PHPS leads to a composite material composed of a majority of Si$_3$N$_4$ and around 13 wt% of silicium (Si).[45] As PHPS is available in solution (in xylene in the present case) and is highly reactive even at room temperature, the precise measurement of its ceramic yield is difficult because cross-linking inherently occurs at low temperature. As an illustration, the measured weight loss at 1000 °C varies from 16.0% (ref. 45) to 24.7% (ref. 46) in the literature; therefore the ceramic yield is calculated to vary from 75.3% to 84%. Such values, even though they are different, are sufficiently high to keep the maximum of product in the porosity of templates through the nanocasting process meaning that PHPS seems to

be an ideal precursor for preparing materials with tailored porosity which has never been demonstrated.

In the present paper, nanocasting provides access to mesopores by replicating the nanostructure of CMK-3 into a locally ordered pore system through (i) the impregnation of the pore template with PHPS solution (20 wt% in xylene) at 10 °C for 48 h under static vacuum, (ii) the subsequent filtration step that consists to selectively remove the PHPS molecules deposited outside while the capillary forces kept the PHPS molecules effectively inside the pores, (iii) the post-treatment of the infiltrated template at low pressure and 30 °C in order to slowly remove the solvent while PHPS crosslinks, (iv) the pyrolysis under nitrogen at 1000 °C (dwelling time of 2 h) of the composite PHPS/CMK-3 to convert the PHPS confined in the porosity of CMK-3 into a composite Si$_3$N$_4$/Si, and (v) the heat-treatment under ammonia (dwelling time of 5 h) to remove CMK-3 involving a weight loss of 54.5% while the title sample is generated.

The thermogravimetric curve in Fig. 3a shows that the template is eliminated at high temperature above 800 °C. At this temperature, the ceramic conversion of PHPS is almost achieved. Within this context, we tentatively performed the heat-treatment of the composite PHPS/CMK-3 directly under ammonia (dwelling time of 5 h) to convert PHPS into a ceramic while the template was removed. This allowed us to reduce the number of steps in the process. In that case, a hydrogenated compound with composition close to Si$_3$N$_4$ is obtained.[47] We obtained a nitrogen adsorption–desorption isotherms of IV-type similarly to mesoporous materials with a specific surface of 715.8 m^2 g^{-1}, a mean pore size of 4.85 nm (with a certain proportion of macropores) and a pore volume of 0.94 cm^3 g^{-1} (Fig. 1SI, see ESI†). Because of values slightly lower than those obtained with the two-step heat-treatment (see later) and the presence of macropores, we focused on the samples labeled *omp*-Si$_3$N$_4$ obtained with the two-step heat-treatment described above and illustrated in Fig. 2.

B Characterization of ordered mesoporous Si$_3$N$_4$ nanoblocks

As-obtained samples are X-ray amorphous based on the absence of diffraction peaks in their powder X-ray Diffraction (XRD) pattern (Fig. 3b) and they are generated as highly porous powders that are composed of agglomerated elongated blocks as shown in the Scanning Electron Microscopy (SEM) image (Fig. 3b as inset). They display a typical chemical formula determined by Energy Dispersive X-ray Spectroscopy (EDXS) of Si$_{3.0}$O$_{0.1}$N$_{4.4}$. The relatively low O content is related to the precautions which are taken to analyze the material: samples are kept in an argon-filled glove-box to avoid moisture adsorption. Furthermore, CMK-3 was heat-treated under vacuum to remove moisture before impregnation of PHPS. Here, there is no residual carbon and no excess of Si: the Si : N ratio is almost that one found in Si$_3$N$_4$. It should be mentioned that the Si : N ratio is around 1 after the first step of the process under nitrogen at 1000 °C (chemical composition of the sample is Si$_{3.0}$N$_{2.9}$O$_{0.1}$ by EDXS). This means that the second treatment under ammonia allows removing CMK-3 while nitridation of
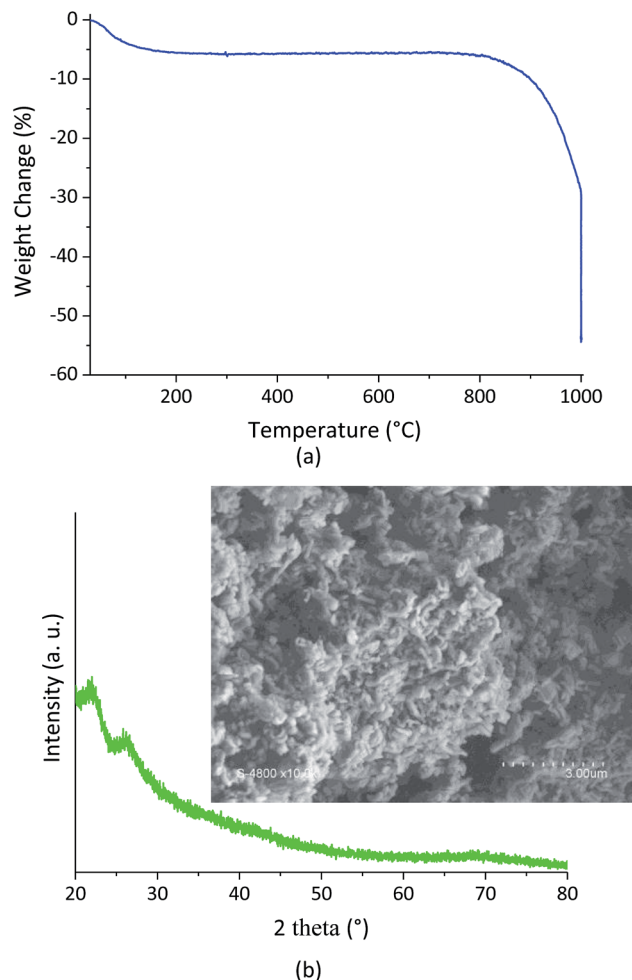
(a)

(b)

Fig. 3 (a) TGA curves of PHPS-derived Si_3N_4@CMK-3 recorded during decomposition under ammonia at 1000 °C (5 °C min^{-1}), (b) XRD patterns and SEM picture of *omp*-Si_3N_4.

(a)

(b)

Fig. 4 (a) Low and (b) high magnification TEM images of *omp*-Si_3N_4.

the silicon present in the material after thermal conversion of PHPS under nitrogen at 1000 °C occurs to form near-stoichiometric Si_3N_4.[48] The absence of carbon is confirmed by the heat-treatment in air of the sample which does not exhibit any weight change in the temperature domain where CMK-3 is oxidized (350–550 °C, Fig. 2SI, see ESI†). Fig. 4a and b depicts the corresponding low and high magnification Transmission Electron Microscope (TEM) images of the sample.

To confirm the TEM observations, the samples have been analyzed by Small-Angle X-ray Diffraction (SA-XRD), Small-Angle X-ray Scattering (SAXS) and nitrogen gas adsorption–desorption measurements (Fig. 5).

The SA-XRD pattern confirms the ordered structure of the specimens (Fig. 5a). A clear diffraction peak at $2\theta = 1.39°$ corresponding to $d = 6.35$ nm is observed. This peak is assigned to the (100) reflection of the 2D hexagonal lattice (space group $P6mm$) with a lattice parameter $a_{100} = 7.3$ nm. Other peaks characteristic of the hexagonal structure and observed in CMK-3 do not appear because of a partial loss of the order in *omp*-Si_3N_4 due to the impregnation-heat-treatment cycle which inherently involves loss of matter. The SAXS pattern of *omp*-Si_3N_4 (Fig. 5a
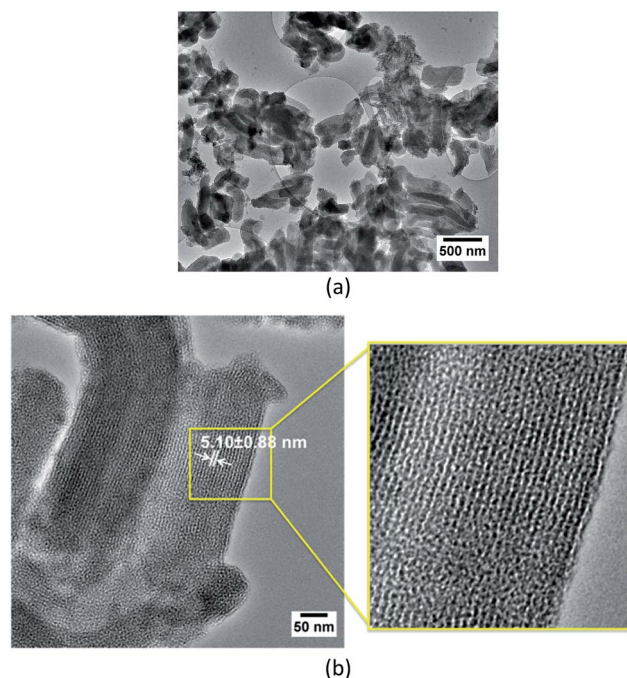
as inset) that displays a well-resolved (100) peak at the q vector of 0.99 also demonstrates the presence of ordered hexagonal pore arrays with mesoporous structure. The analysis of the nitrogen adsorption–desorption isotherms of *omp*-Si_3N_4 (Fig. 5b) allows to estimate the pore-network dimension and structure of nanoblocks. The isotherms show IV-type-curves in which the adsorption and desorption isotherms do not coincide over the region of relative pressure $P/P_0 = 0.4$–0.72. The IV-type isotherms suggest that the samples have uniform mesoporous channels.[49] At relative pressure below 0.1, the relatively high uptake implies the presence of micropores. The type of the adsorption hysteresis is relatively complex and usually speculative. We can suggest that it represents a mixture of H1-type (typical for SBA-15 (ref. 50)) and H2-type which is due to the interconnectivity of the pores.[51] Therefore, we can consider that *omp*-Si_3N_4 samples are mesoporous materials with interconnected pores. A specific BET surface area as high as 772.4 m^2 g^{-1} is measured. The total pore volume determined from the amount of nitrogen adsorbed at $P/P_0 = 0.97$ is as high as 1.19 cm^3 g^{-1}. The pore size distribution (PSD) was calculated from the desorption branch by means of the Barett–Joyner–Halenda method. A uniform diameter of 4.83 nm is found (Fig. 5b as inset). In comparison to the textural properties of CMK-3, the values are logically lower but they are in the range of the highest values reported for PDCs to our knowledge. This means that the PHPS solution is efficiency infiltrated in the porosity of CMK-3 most probably due its low viscosity and the good wettability. The high BET surface area, tailored mesoporous structure and large pore volume of *omp*-Si_3N_4 are also the results of the high ceramic yield of PHPS. These textural characteristics are positive features for heterogeneous catalysis and in particular, they are beneficial to the growth of
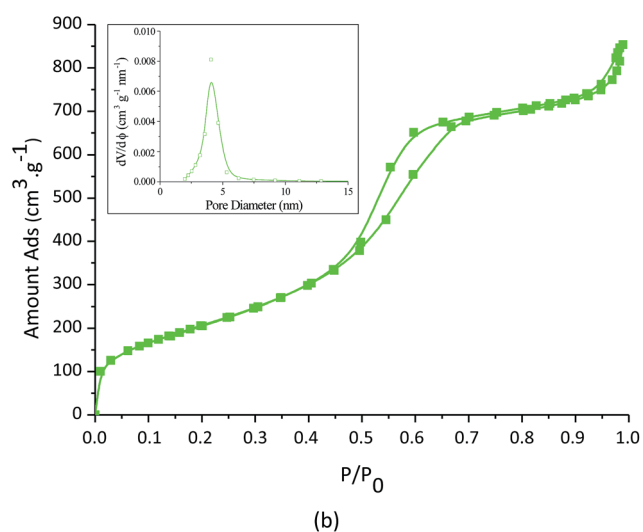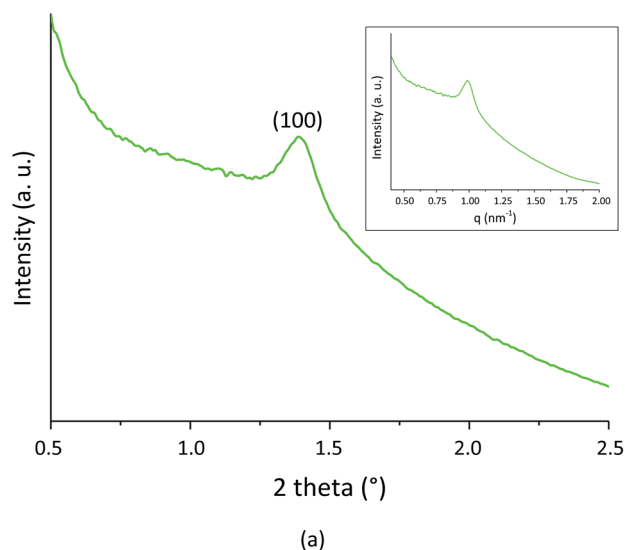
(a)

(b)

Fig. 5 (a) SA-XRD and SAXS patterns (as inset), (Cu Kα radiation) and (b) N₂ adsorption–desorption isotherms recorded at 77 K of *omp*-Si₃N₄. Pore size distribution as inset.

monodisperse Pt nanoparticles for the catalytic hydrolysis of NaBH₄ which is investigated in the following section.

C Preparation and characterization of the nanocatalysts

Pt nanoparticles are deposited on *omp*-Si₃N₄ using hexahydrated chloroplatinic acid as precursor by wet impregnation followed by chemical reduction in alkaline medium. This generated a nanocatalyst labeled Pt/*omp*-Si₃N₄ which could be used to catalytically activate the hydrolysis of NaBH₄. The successful loading of Pt on *omp*-Si₃N₄ giving the sample Pt/*omp*-Si₃N₄ has been verified by TEM, EDXS and elemental mapping (Fig. 6).

TEM images of Pt/*omp*-Si₃N₄ are shown in Fig. 6a and b (as inset). We clearly observe a majority of homogeneously dispersed Pt nanoparticles with a spherical shape on the surface of the Si₃N₄ nanoblocks (Fig. 6a and marked with white arrows) and a few ones that tend to agglomerate are found (circle). The
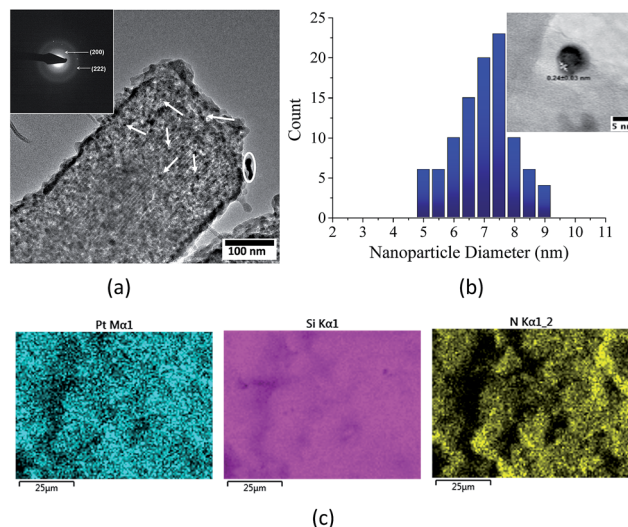

(a) (b) (c)

Fig. 6 (a and b) TEM images and particle size distribution, and (c) elemental mapping of Pt/*omp*-Si₃N₄.

omp-Si₃N₄ sample does not show any crystallinity in the Selected Area Electron Diffraction (SAED) pattern (Fig. 6 as inset) confirming its amorphous structure as previously observed by XRD. Once Pt is impregnated, we observe a few spots and extremely diffuse rings belonging to Pt, which crystallizes in the fcc system. We identified the (200) and (222) crystalline planes of fcc Pt, according to a direct comparison with the values specified in the crystallographic database. The rings are not more pronounced due to the prominent amorphous character of the Si₃N₄ substrate and the scarce loading of Pt nanoparticles on the selected area. Fig. 6b shows one Pt nanoparticle supported on the surface of the nanoblocks in a ⟨110⟩ orientation. Lattice fringes are clearly distinguishable, emphasizing a lattice spacing of 0.24 ± 0.03 nm, which corresponds to the (111) crystalline planes of Pt. The mean size of the Pt nanoparticles distributed on the surface of *omp*-Si₃N₄ has been found to be 6.77 nm, as shown in the histogram of the nanoparticles diameters, for which we have considered 100 nanoparticles (Fig. 6b). The histogram emphasizes the low size distribution of the NPs (comprised between 5–9 nm), which confirms that the support contains a homogeneous size distribution of mesopores. Then cross-sections were prepared by using a focused ion beam unit, and EDXS maps were superimposed on the cross-sectional images (Fig. 3SI, see ESI†). Elemental mapping (Fig. 6d) reveals the uniform distribution of silicon and nitrogen from the support as well as Pt on *omp*-Si₃N₄. EDXS spectroscopy indicates the presence of 0.61 wt%.

After Pt growth, the shape of the isotherms and the hysteresis loop of Pt/*omp*-Si₃N₄ (Fig. 4SI, see ESI†) are similar to the isotherms of the parent *omp*-Si₃N₄ revealing that the highly ordered structure is maintained even after deposition and/or encapsulation of the Pt nanoparticles. The specific BET surface was found to decrease by only 25–30% from 772.4 m² g⁻¹ to 586.7 m² g⁻¹. These results are clearly attributed to the formation of the nanoparticles inside the pore channels. However, the absence of an abrupt change in the surface area of

the support after Pt growth further proves that the pores of the support are not blocked by nanoparticles larger than the pore size of the support, revealing that this support in general hinders the agglomeration or migration of the nanoparticles. This is also fundamental to allow diffusion of the borates through the porosity.

The activity of Pt/omp-Si$_3$N$_4$ for the hydrolysis of sodium borohydride was investigated at 80 °C, in a very alkaline solution (pH > 10), and with the presence of water. It is important to mention that the catalytic ability of the Pt-free supports omp-Si$_3$N$_4$ was assessed and, as expected, they were found to be inactive. The hydrogen generation results for Pt/omp-Si$_3$N$_4$ are presented in Fig. 7. It should be mentioned that there is usually a lack of direct comparison on the catalytic performance among mesoporous supports. As a consequence, this renders difficult to pinpoint which is the best composition for H$_2$ generation or which parameters are critical for an efficient process. Therefore, we decided to compare the Pt/omp-Si$_3$N$_4$ nanocatalyst firstly with a Pt/omp-Si/Al/C/N nanocatalyst. The latter is prepared through the same process using PHPS as a precursor.[40] omp-Si/Al/C/N represents an ordered mesoporous silicon aluminum carbonitride sample with a SSA of 326 m^2 g^{-1} and a pore volume of 0.61 cm^3 g^{-1}. The idea behind the preparation of this sample is to follow the effect of textural parameters (SSA and pore volume) on the quantity of hydrogen which is generated during the hydrolysis of NaBH$_4$. Secondly, we synthesized a Pt-supported CMK-3 (SSA = 983 m^2 g^{-1}, Table 1) labeled Pt/CMK-3 through the same process we applied to prepare Pt/omp-Si$_3$N$_4$. CMK-3 was the template used to prepare omp-Si$_3$N$_4$. Our objective was to assess the advantage of using or not PDCs as catalytic supports for the catalytic hydrolysis of NaBH$_4$ in the severe conditions we imposed.

Using the Pt/omp-Si$_3$N$_4$ nanocatalyst, the hydrolysis starts immediately; no induction period is observed, which is in agreement with the metallic state of Pt as the occurrence of an induction period is generally observed with oxidized metals.[10] A

hydrogen generation rate (slope of the curves at a conversion <50%) of 1.3 mL min^{-1} was measured. Expressed per gram of Pt, the rate is 13.54 L min^{-1} g$_{Pt}^{-1}$, which is a high performance, especially when compared to many of the supported platinum catalysts reviewed elsewhere.[52] A direct comparison to the literature is somehow complicated because of the discrepancies in the experimental conditions, but it may give a good idea about the aforementioned performance. For example, hydrogen generation rates of 0.2, 0.7 and 1.6 L min^{-1} g$_{Pt}^{-1}$ in the presence of 1 wt% Pt/γAl$_2$O$_3$, 1 wt% Pt/C and 1 wt% Pt/TiO$_2$, respectively, were reported at 40 °C for diluted NaBH$_4$ solutions.[53]

To highlight the performance of Pt/omp-Si$_3$N$_4$, it seems better to test other materials, $i.e.$, Pt/omp-Si/Al/C/N (with 0.8 wt% of Pt as measured by EDXS) and Pt/CMK-3 (with 0.91 wt% of Pt as measured by EDXS), in the same conditions and for the same reaction (Fig. 7). The hydrogen evolution profile using the Pt/omp-Si/Al/C/N nanocatalyst is kinetically lower. Expressed per gram of Pt, the rate is calculated to be 5.67 L min^{-1} g$_{Pt}^{-1}$, which is a significantly lower performance most probably attributed to the textural parameters (SSA and pore volume) of the supports: the SSA and pore volume values of omp-Si/Al/C/N are significantly lower than those of omp-Si$_3$N$_4$. The hydrogen evolution of the Pt/CMK-3 nanocatalyst is markedly different from that observed with the Si$_3$N$_4$-based nanocatalyst. During the first minutes, the hydrogen release is fast: this is explained by the catalytic activity of the Pt nanoparticles as well as some contribution of the acid groups available on the surface of the carbonaceous support. However, this fast step is soon followed by a process with slow kinetics. Visual inspection of the reactor showed that the carbonaceous support favorably adsorbs water and significantly swells. The consequence is that the diffusion of the anions BH$_4^-$ and B(OH)$_4^-$ is negatively affected; accordingly, the surface reactions are restricted, the borates desorption is hindered (leading to a catalyst surface "poisoning") and the hydrolysis kinetics are decreased. Expressed per gram of Pt, the hydrogen evolution rate is as low as 2.58 L min^{-1} g$_{Pt}^{-1}$. In other words, the adsorption/swelling ability of carbon is a drawback in our experimental conditions (excess of water and high temperature) as it leads to harsh experimental conditions in the vicinity of the platinum nanoparticles, which makes then the catalytic reaction more challenging. In contrast, these phenomena do not appear with the Pt/omp-Si$_3$N$_4$ nanocatalysts. As a matter of fact, omp-Si$_3$N$_4$ is a most suitable support for the aforementioned reaction. Considering the recyclability of the borates, the proposed nanocatalyst may be viewed as an effective hydrogen source to meet the overall energy requirements for civil vehicles applications such as for small Unmanned Aerial Vehicles (UAVs). However, these nanoblocks have necessary some difficulties in practical use, $i.e.$ in the scale of the demonstrator reactor. Recently, Seven $et al.$ proposed the use of monolithic cryogel supported Co and Ni catalysts.[54] Porous cryogels were prepared from poly(acrylamide). However, in the conditions we impose, the use of these cryogels can be problematic. Within this context, further investigations are under progress to prepare monolithic Si$_3$N$_4$ with different types of porosity as well as other forms of PDCs. In particular, porous felts obtained by
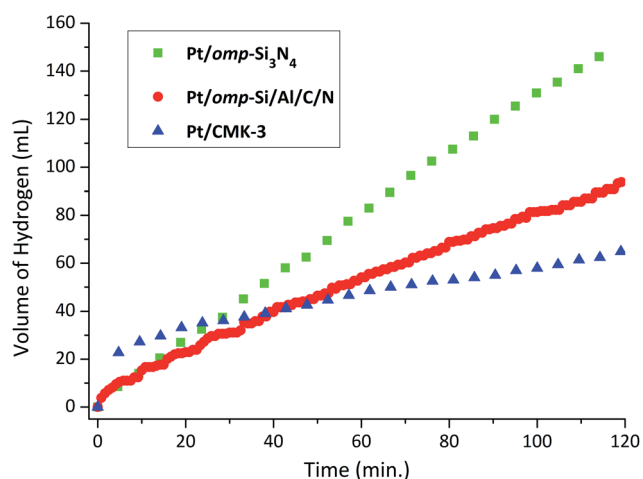

Fig. 7 Hydrogen generation by hydrolysis of sodium borohydride at 80 °C over Pt-based nanocatalysts.

electrospinning preceramic polymers[55–57] are promising. These materials, the related metal supported monoliths, their catalytic performance and their reusability in operating conditions will be published separately.

D Conclusions

Highly ordered mesoporous silicon nitride (Si_3N_4) with a *P6mm* hexagonal symmetry has been synthesized in the form of nanoblocks by polymer nanocasting using mesoporous carbon (CMK-3) as hard template and perhydropolysilazane (PHPS) as Si_3N_4 precursor. The solution infiltration-ceramic conversion-template removal cycle performed under nitrogen then ammonia at 1000 °C resulted in the formation of periodic mesoporous amorphous Si_3N_4 nanoblocks with surface areas as high as 772.4 m^2 g^{-1}, a pore size distribution of 4.83 nm and a pore volume of 1.19 cm^3 g^{-1}. Nanoblocks have been used as supports to nucleate platinum nanoparticles (6.77 nm in mean size) leading to nanocatalysts to be successfully assessed for hydrolysis of an alkaline aqueous solution of sodium borohydride ($NaBH_4$) at 80 °C. High H_2 rate has been measured (13.54 L min^{-1} g_{Pt}^{-1}). The performance is even significantly superior to that obtained with other ordered mesoporous PDCs and CMK-3 (2.58 L min^{-1} g_{Pt}^{-1}). Considering the recyclability of borates and the intrinsic stability of Si_3N_4 nanoblocks, the new material presented in this work offers interesting performance for the practical implementation of B-/N-based hydrides as a hydrogen source for fuel cell application. Maybe more importantly, this work is also announcing the emergence of the use of non-oxide ceramics and in particular nitride/carbonitride-based ceramics when dealing with heterogeneous catalysis. In particular, an important aspect of the current research is the extension of the underlying application to monoliths with different types of porosity as well as to porous felts.

Acknowledgements

Notes and references

1 A. S. Arico, P. Bruce, B. Scrosati, J. M. Tarascon and W. van Schalkwijk, *Nat. Mater.*, 2005, **4**, 366.

2 M. K. Debe, *Nature*, 2012, **486**, 43.

3 M. Yadav and Q. Xu, *Energy Environ. Sci.*, 2012, **5**, 9698.

4 A. F. Dalebrook, W. Gan, M. Grasemann, S. Moret and G. Laurenczy, *Chem. Commun.*, 2013, **49**, 8735.

5 C. Cento, P. Gislon and P. P. Prosini, *Int. J. Hydrogen Energy*, 2008, **34**, 4551.

6 K. Eom, W. Cho and H. Kwon, *J. Power Sources*, 2008, **180**, 484.

7 S. Peng, X. Fan, J. Zhang and F. Wang, *Appl. Catal., B*, 2013, **140–141**, 115.

8 Y. Kojima, Y. Kawai, H. Nakanishi and S. Matsumoto, *J. Power Sources*, 2004, **135**, 36.

9 D. M. F. Santos and C. A. C. Sequeira, *Renewable Sustainable Energy Rev.*, 2011, **15**, 3980.

10 U. B. Demirci and P. Miele, *Phys. Chem. Chem. Phys.*, 2014, **16**, 6872.

11 U. B. Demirci and P. Miele, *Phys. Chem. Chem. Phys.*, 2011, **13**, 3809.

12 M. Zahmakiran and S. Özkar, *Langmuir*, 2009, **25**, 2667.

13 C. Zhang and J. A. Lercher, *Angew. Chem., Int. Ed.*, 2012, **51**, 5935.

14 Y. H. Huang, C. C. Su, S. L. Wang and M. C. Lu, *Energy*, 2012, **46**, 242.

15 W. Ye, H. Zhang, D. Xu, L. Ma and B. Yi, *J. Power Sources*, 2007, **164**, 544.

16 R. Chamoun, U. B. Demirci, D. Cornu, Y. Zaatar, A. Khoury, R. Khoury and P. Miele, *Appl. Surf. Sci.*, 2010, **256**, 7684.

17 M. Pourbaix, *Atlas of Electrochemical Equilibria in Aqueous Solutions*, National Association of Corrosion Engineers, Houston, TX, USA, 1974.

18 R. M. Ravenelle, F. Schuessler, A. D'Amico, N. Danilina, J. A. van Bokhoven, J. A. Lercher, C. W. Jones and C. Sievers, *J. Phys. Chem. C*, 2010, **114**, 19582.

19 A. Corma, H. Garcia, I. Liabres and F. X. Xamena, *Chem. Rev.*, 2010, **110**, 4606.

20 Ö. Metin, S. Özkar and S. Sun, *Nano Res.*, 2010, **3**, 676–684.

21 C. Methivier, J. Massardier and J. C. Bertolini, *Appl. Catal., A*, 1999, **182**, 337.

22 F. Monnet, Y. Shuuman, F. J. Cadete Santos Aires, J. C. Bertolini and C. Mirodatos, *Catal. Today*, 2001, **64**, 51.

23 F. J. Cadete Santos Aires, I. Kurzina, G. Garcia Cervantes and J. C. Bertolini, *Catal. Today*, 2006, **117**, 518.

24 F. J. Cadete Santos Aires, G. Garcia Cervantes and J. C. Bertolini, *Catal. Lett.*, 2009, **129**, 266.

25 A. S. Blokhina, I. A. Kurzina, V. I. Sobolev, K. Y. Koltunov, G. V. Mamontov and O. V. Vodyankina, *Kinet. Catal.*, 2012, **53**, 477.

26 (*a*) F. Cheng, S. M. Kelly, N. A. Young, S. Clark, M. G. Francesconi, F. Lefebvre and J. S. Bradley, *Chem. Commun.*, 2005, 5662; (*b*) F. Cheng, S. M. Kelly, N. A. Young, C. N. Hope, K. Beverley, M. G. Francesconi, S. Clark, J. S. Bradley and F. Lefebvre, *Chem. Mater.*, 2006, **18**, 5996.

27 M. Kamperman, A. Burns, R. Weissgraeber, N. V. Vegten, S. C. Warren, S. M. Gruner, A. Baiker and U. Wiesner, *Nano Lett.*, 2009, **9**, 2756.

28 (*a*) G. Glatz, T. Schmalz, T. Kraus, F. Haarmaan, G. Motz and R. Kempe, *Chem.–Eur. J.*, 2010, **16**, 4231; (*b*) M. Zaheer, C. D. Keenan, J. Hermannsdörfer, R. Roessler, G. Motz, J. Senker and R. Kempe, *Chem. Mater.*, 2012, **24**, 3952; (*c*) M. Zaheer, T. Schmalz, G. Motz and R. Kempe, *Chem. Soc. Rev.*, 2012, **41**, 5102; (*d*) M. Zaheer, J. Hermannsdörfer,

W. P. Kretschmer, G. Motz and R. Kempe, *ChemCatChem*, 2014, **6**, 91.

29 (*a*) M. S. Bazarjani, H.-J. Kleebe, M. M. Müller, C. Fasel, M. B. Yazdi, A. Gurlo and R. Riedel, *Chem. Mater.*, 2011, **23**, 4112; (*b*) M. S. Bazarjani, M. M. Müller, H.-J. Kleebe, Y. Jüttke, I. Voigt, M. B. Yazdi, L. Alff, R. Riedel and A. Gurlo, *ACS Appl. Mater. Interfaces*, 2014, **6**, 12270.

30 (*a*) O. Majoulet, M. C. Bechelany, F. Sandra, G. Bonnefont, G. Fantozzi, L. Joly-Pottuz, A. Malchere, S. Bernard and P. Miele, *J. Mater. Chem. A*, 2013, **1**, 10991; (*b*) S. Bernard, O. Majoulet, F. Sandra, A. Malchere and P. Miele, *Adv. Eng. Mater.*, 2013, **15**, 134.

31 P. Krawiec, D. Geiger and S. Kaskel, *Chem. Commun.*, 2006, 2469.

32 Y. Shi, Y. Wan, B. Tu and D. Zhao, *J. Phys. Chem. C*, 2008, **112**, 112.

33 S. Bernard and P. Miele, *New J. Chem.*, 2014, **38**, 1923.

34 O. Majoulet, J. G. Alauzun, L. Gottardo, C. Gervais, M. E. Schuster, S. Bernard and P. Miele, *Microporous Mesoporous Mater.*, 2011, **140**, 40.

35 Y. Shi, Y. Wan and D. Zhao, *Chem. Soc. Rev.*, 2011, **40**, 3854.

36 L. Borchardt, C. Hoffman, M. Oschatz, L. Mammitzsch, U. Petasch, M. Hermann and S. Kaskel, *Chem. Soc. Rev.*, 2012, **41**, 5053.

37 (*a*) J. G. Alauzun, S. Ungureanu, N. Brun, S. Bernard, P. Miele, R. Backov and C. Sanchez, *J. Mater. Chem.*, 2011, **21**, 14025; (*b*) S. Schlienger, J. Alauzun, F. Michaux, L. Vidal, J. Parmentier, C. Gervais, F. Babonneau, S. Bernard, P. Miele and J. B. Parra, *Chem. Mater.*, 2012, **24**, 88.

38 S. Kaskel, K. Schlichte and B. Zibrowius, *Phys. Chem. Phys. Chem. Phys.*, 2002, **4**, 1675.

39 (*a*) M.-C. Bechelany, V. Proust, C. Gervais, R. Ghisleny, S. Bernard and P. Miele, *Adv. Mater.*, 2014, **26**, 6548; (*b*) G. Mera, M. Gallei, S. Bernard and E. Ionescu, *Nanomaterials*, 2015, **5**, 468; (*c*) Z. Xie, S. Cao, J. Wang, X. Yan, S. Bernard and P. Miele, *Mater. Sci. Eng., A*, 2010, **527**, 7086.

40 O. Majoulet, C. Salameh, M. E. Schuster, U. B. Demirci, Y. Sugahara, S. Bernard and P. Miele, *Chem. Mater.*, 2013, **25**, 3957.

41 O. Akdim, U. B. Demirci and P. Miele, *Int. J. Hydrogen Energy*, 2011, **36**, 13669.

42 D. Seyferth, G. H. Wiseman and C. Prud'homme, *J. Am. Ceram. Soc.*, 1983, **66**, C-13.

43 C. R. Blanchard and S. T. Schwab, *J. Am. Ceram. Soc.*, 1994, **77**, 1729.

44 Y. Iwamoto, W. Völger, E. Kroke and R. Riedel, *J. Am. Ceram. Soc.*, 2001, **84**, 2170.

45 M. Günther, T. Kraus, A. Diendorf, D. Decker, W. Krenkel and G. Motz, *J. Eur. Ceram. Soc.*, 2009, **29**, 2061.

46 Y. Mori, T. Ueda, S. Kitaoka and Y. Sugahara, *J. Ceram. Soc. Jpn.*, 2006, **114**, 497.

47 O. Funayama, Y. Tashiro, A. Kamo, M. Okumura and T. Isoda, *J. Mater. Sci.*, 1994, **29**, 4883.

48 (*a*) S. P. Murarka, C. C. Chang and A. C. Adams, *J. Electrochem. Soc.*, 1979, **126**, 996; (*b*) R. C. Anderson, R. S. Müller and C. W. Tobias, *J. Electrochem. Soc.*, 1993, **140**, 1393.

49 (*a*) K. S. W. Sing, *Pure Appl. Chem.*, 1985, **57**, 603; (*b*) J. Rouquerol, D. Avnir, C. W. Fairbridge, D. H. Everett, J. M. Haynes, N. Pernicone, J. D. F. Ramsay, K. S. W. Sing and K. K. Unger, *Pure Appl. Chem.*, 1994, **66**, 1739.

50 R. Pitchumani, W. Li and M.-O. Coppers, *Catal. Today*, 2005, **105**, 618.

51 G. Masson, *J. Colloid Interface Sci.*, 1982, **88**, 36.

52 U. B. Demirci, O. Akdim, J. Andrieux, J. Hannauer, R. Chamoun and P. Miele, *Fuel Cells*, 2010, **10**, 335.

53 V. I. Simagina, P. A. Storozhenko, O. V. Netskina, O. V. Komova, G. V. Odegova, T. Y. Samoilenko and A. G. Gentsler, *Kinet. Catal.*, 2007, **48**, 168.

54 F. Seven and N. Sahiner, *J. Power Sources*, 2014, **272**, 128.

55 J. Wilfert, R. von Hagen, R. Fiz, M. Jansen and S. Mathur, *J. Mater. Chem.*, 2012, **22**, 2099.

56 T. Gerges, V. Salles, S. Bernard, C. Journet, X. Jaurand, R. Chiriac, G. Ferro and A. Brioude, *Nanotechnology*, 2015, **26**, 085603.

57 V. Salles, S. Bernard, A. Brioude, D. Cornu and P. Miele, *Nanoscale*, 2010, **2**, 215.